Supplemental Document

Optics EXPRESS

Multi-dimensional wavefront sensing using volumetric meta-optics: supplement

CONNER BALLEW, GREGORY ROBERTS, AND ANDREI FARAON*

Kavli Nanoscience Institute and Thomas J. Watson Sr. Laboratory of Applied Physics, California Institute of Technology, Pasadena, California 91125, USA
faraon@caltech.edu

Supplement DOI: https://doi.org/10.6084/m9.figshare.23906151

Parent Article DOI: https://doi.org/10.1364/OE.492440

Multi-dimensional wavefront sensing using volumetric meta-optics: supporting information

Conner Ballew, Gregory Roberts, and Andrei Faraon*

Kavli Nanoscience Institute and Thomas J. Watson Sr. Laboratory of Applied Physics, California Institute of Technology, Pasadena, California 91125, USA

E-mail: faraon@caltech.edu

S1 Illustration of design procedure

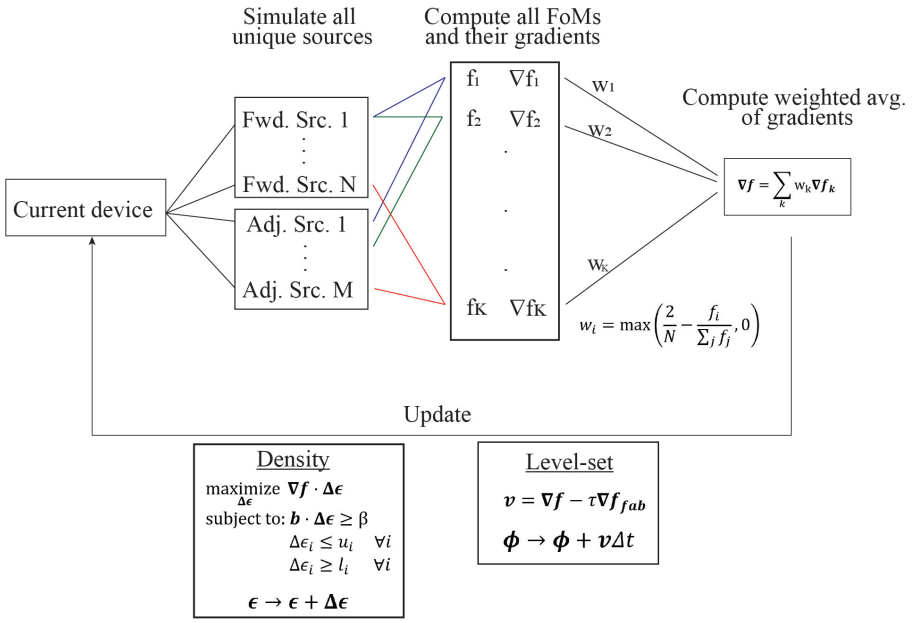

Figure S1: An overview of the design methodology described in the main manuscript. For each iteration the process combines the results of multiple FDTD simulations, denoted forward and adjoint sources, to compute the gradient of many different FoMs. The various gradients are combined and used to update the structure using either a density-based method[1] or a level-set method.[2]

.

S2 Level-set optimization

The term level-set optimization stems from treating the device boundaries as the zero-level contour of a level-set function $\phi(x, y)$. The level-set function (LSF) is perturbed in accordance with the gradient, which has the effect of perturbing the zero-level contour of the LSF and the associated device boundaries to increase performance. We use a signed-distance function to define the level-set function (LSF), where the value of $\phi(x, y)$ is proportional to the signed distance from the device boundary. The gradients of the electromagnetic FoM and a fabrication penalty function are combined and used to perturb the LSF, which has the effect of perturbing the boundary of the device such that the electromagnetic FoM is increased and the fabrication penalty term is decreased. The fabrication penalty term includes both a minimum radius of curvature constraint and a minimum gap size constraint of 60 nm. The LSF is then recomputed to ensure it remains a signed-distance function. This process is repeated until the FoM has converged (recovering the performance lost from the binarization step), and the fabrication penalty term is minimized.

It is critical that we preserve fabrication restrictions during the level-set optimization, and we do so here using the techniques described in detail in Ref.[2] To briefly summarize that work, a multi-dimensional fabrication penalty function is first analytically computed over the entire device region. This function includes two types of fabrication constraints: one limits the radius of curvature of the device boundaries, and the other limits the smallest gap size of the device. The terms are integrated over the entire design region, yielding a real number (the fabrication penalty term) that we wish to minimize. The gradient of this fabrication penalty term is computed over the device region using a finite-difference approximation and is subsequently combined with the gradient of the electromagnetic FoM that is computed through the adjoint method. The level-set function is perturbed in the direction of this combined gradient, resulting in a shifting of the material boundaries that co-optimizes the electromagnetic FoM and the fabrication penalty term.

S3 Convergence plots

The convergence plots showing the average device figure of merit (FoM) and device binarization are shown in Fig. S2. The FoM being plotted is the power transmission through the appropriate pixel. It is worth noting that this is different from the FoM that is used to define the adjoint source, which is the intensity at the center of the appropriate pixel.

The density-based optimization is considered converged when the binarization, which is defined by Eq. 1 of the main manuscript, is nearly 100%. At various points the binarization is forced to increase by passing the permittivity through a sigmoidal function and changing the device permittivity to the output of this function. The FoM is then allowed to recover before repeating this discrete push in binarization. At iteration 512 the optimization switches to a level-set optimization, which recovers some of the performance that was lost during the final phases of the density optimization. During the level-set optimization, the binarization is recorded as approximately 90% because the boundaries of the device are smoothed out yielding a continuous permittivity value. This can intuitively be thought of as the level-set function passing through a simulation mesh voxel, which is modelled in the FDTD simulation as a dielectric volume average of the two materials. Therefore the density optimization is overly restrictive at binarization values above 90%, since it does not allow for this type of border smoothing, instead modelling the device as a discretized grid of binary voxels. This explains why the level-set function is able to recover substantially more performance than what is lost at the initial conversion from density-based optimization to a level-set optimization, recovering to approximately the same average FoM value as the density-based optimization when it was 90% binary.

A non-intuitive aspect of this convergence plot is the FoM being permitted to decrease during the density-phase of the optimization. The reason for this is described in detail in Ref.[1] In short, a hard constraint is imposed that forces binarization to increase, thus forcing the device to tend towards a binary device while either maximizing or minimally sacrificing the FoM using the gradient information from the adjoint-retrieval process.

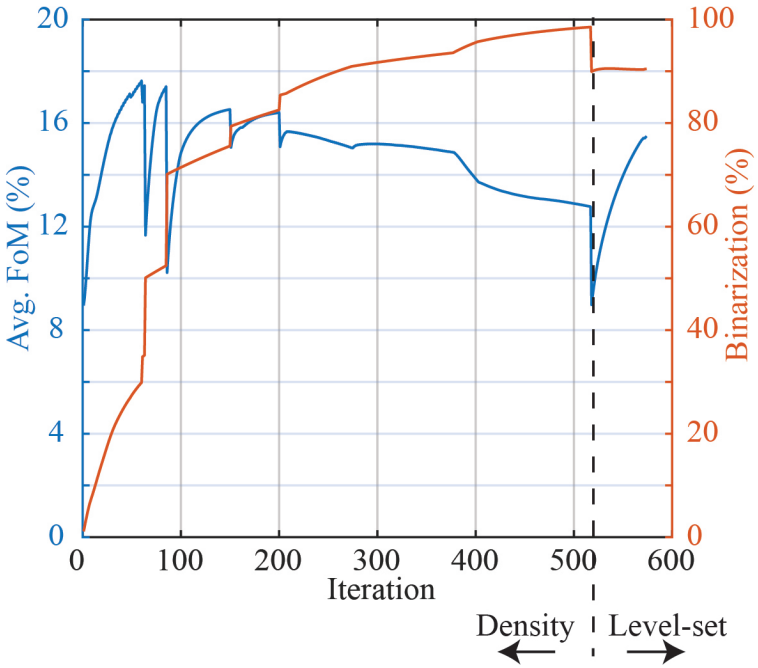

Figure S2: **Convergence plots of the 3D metaoptics device.** The initial density-based optimization features numerous points at which the binarization of the device is forced to increase by passing the current permittivity through a sigmoidal function. At iteration 512 the optimization is converted to a level-set optimization, which recovers the performance lost from that transition. Furthermore, the level-set optimization improves the performance of the device to approximately the same point as when the density-based optimization was 90% binary, which is the approximate binarization when modelled by a level-set curve due to the continuous smoothing of the permittivity at simulation voxels that are intersected by the level-set curve.

S4 Device layers

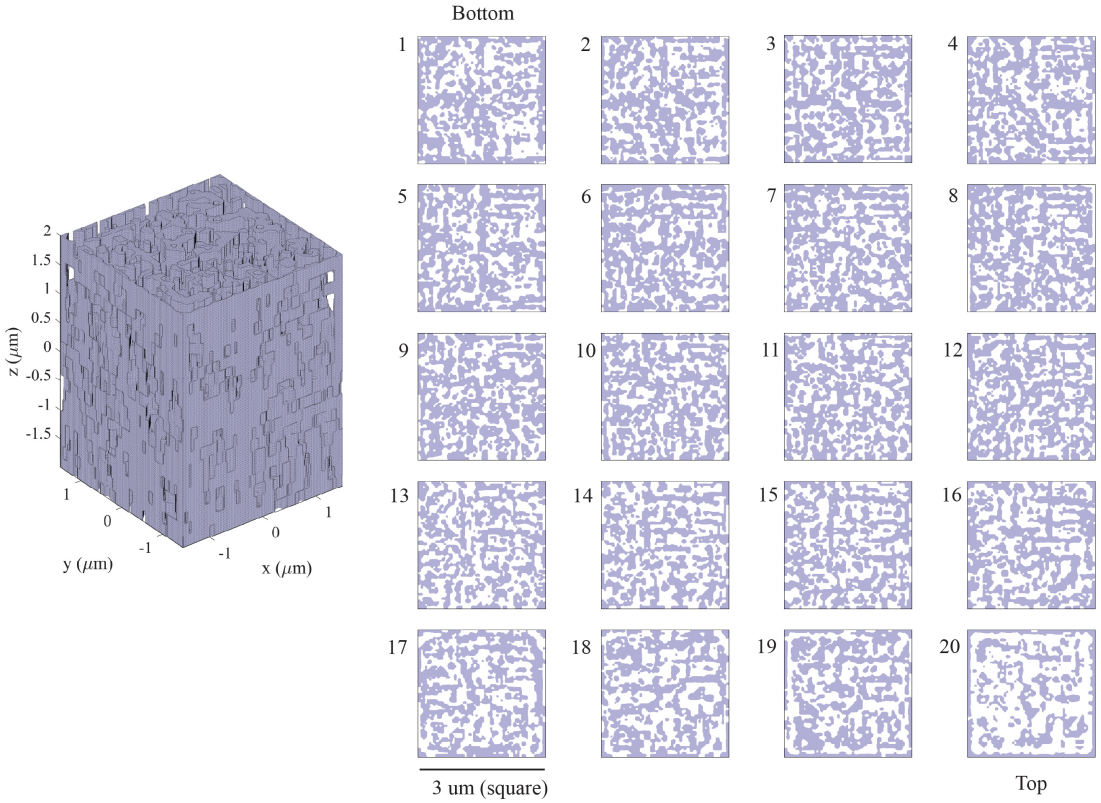

Figure S3: **3D model and device layers.** (Left) A 3D model of the device. The TiO_2 is shaded, and the SiO_2 is transparent. (Right) A detailed view of each layer. The shaded region is TiO_2, and the white is SiO_2. Layer 1 is the bottom layer nearest the sensor array. Each layer is 3x3μm.

S5 Simulation time

A 16-core simulation of the final optimized device presented in the manuscript takes approximately 90 seconds to initialize, run, and save the data on a PC with the following specifications.

- Software: Lumerical FDTD 2022 R1.4
- OS: Windows 10
- Processor: AMD Ryzen Threadripper 3990X 64-Core Processor 2.90 GHz
- RAM: 4x32 GB DDR-4 3200 MHz

This is the time taken to simulate a just one source among the 26 forward and adjoint sources that were used to define all states. The 26 simulations can be done in parallel on computational cluster.

S6 Effects of cross-polarization

The device discussed in the main manuscript sorts incident light based on its polarization, wavelength, and incident angle. The device was designed explicitly for two orthogonal linearly-polarized sources, one polarized in the xz plane and the other in the yz plane. Here, we wish to determine the effect on device performance when excited with planewaves of arbitrary polarization. The response of the device for any polarization state can be determined by coherently summing the electric fields, applying relative amplitude and phase shifts (i.e. a Jones vector) to the two linearly-polarized components to obtain arbitrary elliptical polarizations.

The Jones vector is defined as:

$$\begin{pmatrix} E_{0x} \\ E_{0y}e^{i\phi_J} \end{pmatrix}$$

To sweep the Jones vector over all possibilities, we introduce a variable $\theta_J \in [0, \pi]$ and set $E_{0x} = \cos(\theta_J)$ and $E_{0y} = \sin(\theta_J)$. We then plot the transmission to all pixels as function of (θ_J, ϕ_J) with $\phi_J \in [0, \pi]$. Since we wish to observe interference effects here, we do not average over any properties as was done in quantifying performance in the main manuscript. Instead, the results for all training modes are plotted independently. The transmission to the pixels do exhibit a dependence on the incident angle, but it is not substantial enough to alter the behavior of the device. Thus, the device will exhibit the behavior reported in the main manuscript under any polarization input.

Figures S4-S8 below show these results. θ_J, the relative amplitude, is the x-axis and ϕ_J, the relative phase, is the y-axis for each subplot. Each figure contains the results for all pixels at a particular incident angle (θ, ϕ). The specific pixels to which transmission is *not* maximized are faded. The ordering of the pixels is identical to that of Fig. 1 in the main text. For a high-level interpretation, a table is provided that shows the difference between the maximum and minimum values for each plots, which describes the max variation in transmission to each pixel if the input was swept through every possible polarization state. The variation is large for polarization-sorting pixels as expected, and small for the other functionalities.

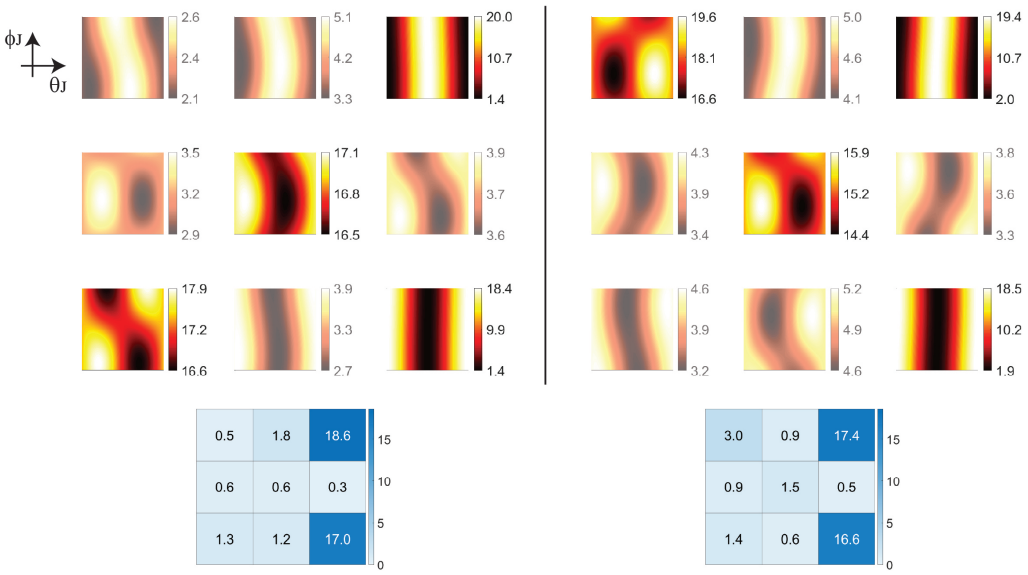

Figure S4: $(\theta, \phi) = (0°, 0°)$. Left set of figures correspond to 620 nm, the right set to 532 nm.

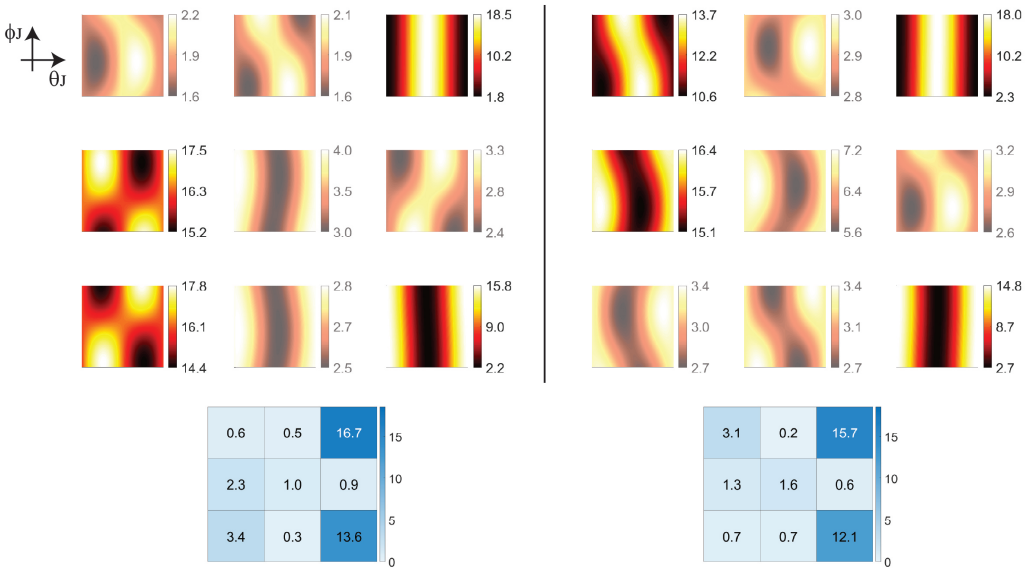

Figure S5: $(\theta, \phi) = (5°, 0°)$. Left set of figures correspond to 620 nm, the right set to 532 nm.

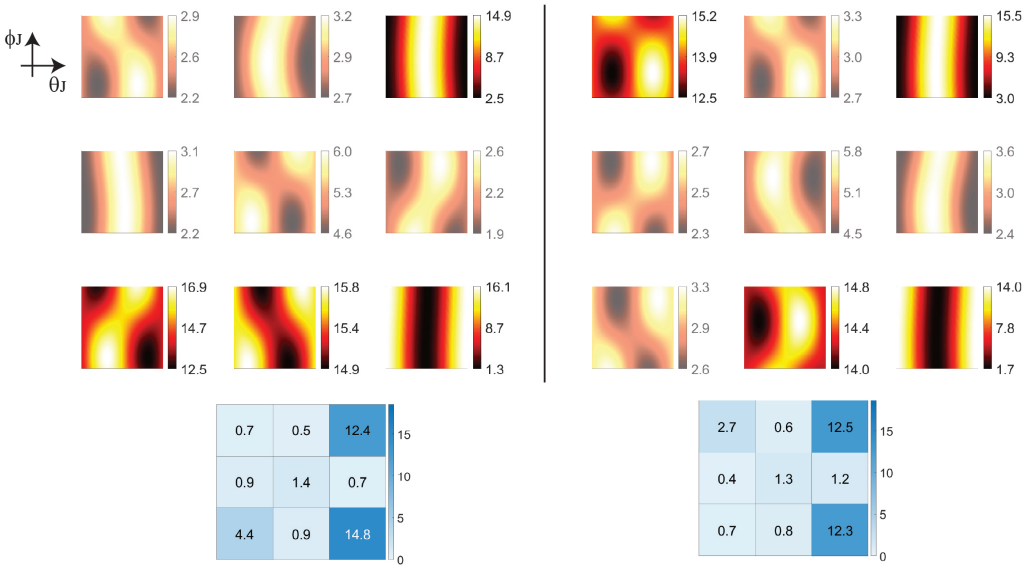

Figure S6: $(\theta, \phi) = (5°, 90°)$. Left set of figures correspond to 620 nm, the right set to 532 nm.

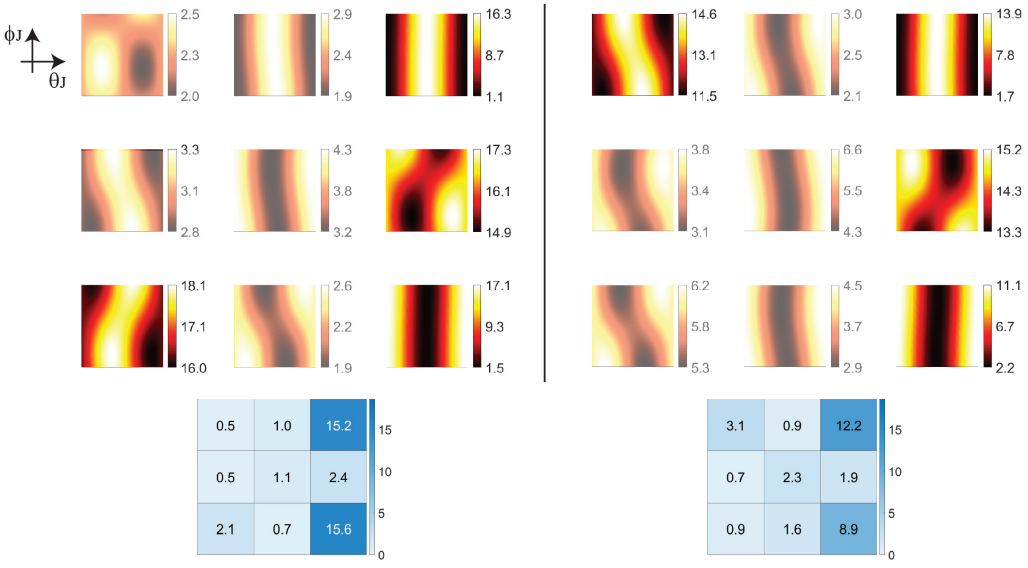

Figure S7: $(\theta, \phi) = (5°, 180°)$. Left set of figures correspond to 620 nm, the right set to 532 nm.

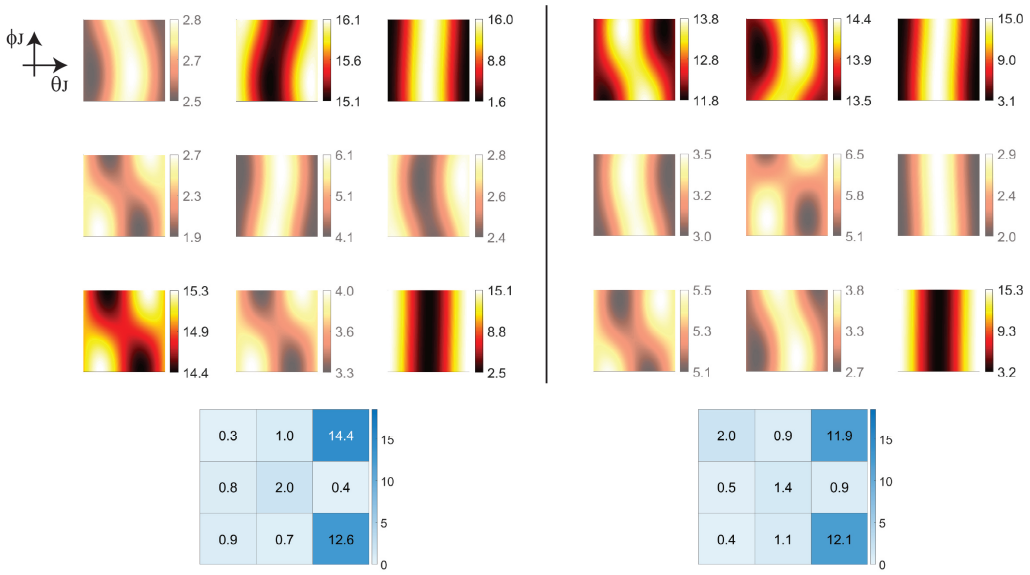

Figure S8: $(\theta, \phi) = (5°, 270°)$. Left set of figures correspond to 620 nm, the right set to 532 nm.

S7 Scrambling pixels

In the main manuscript a comparison is performed between 20 different pixel distributions, and their qualitative behavior is analyzed by cross correlating the angular responses of the pixels with an overlap integral. This procedure is illustrated in Figure S9, and compares the two least similar distribution according to the overlap integral. The least similar functionality was the yz-polarization in this case, and this arises from one device having a maximum at an angle where the other has a minimum. However, both pixels feature relatively uniform transmissions that do not approach zero, so the overlap between the two distributions remains relatively high at 90.5%.

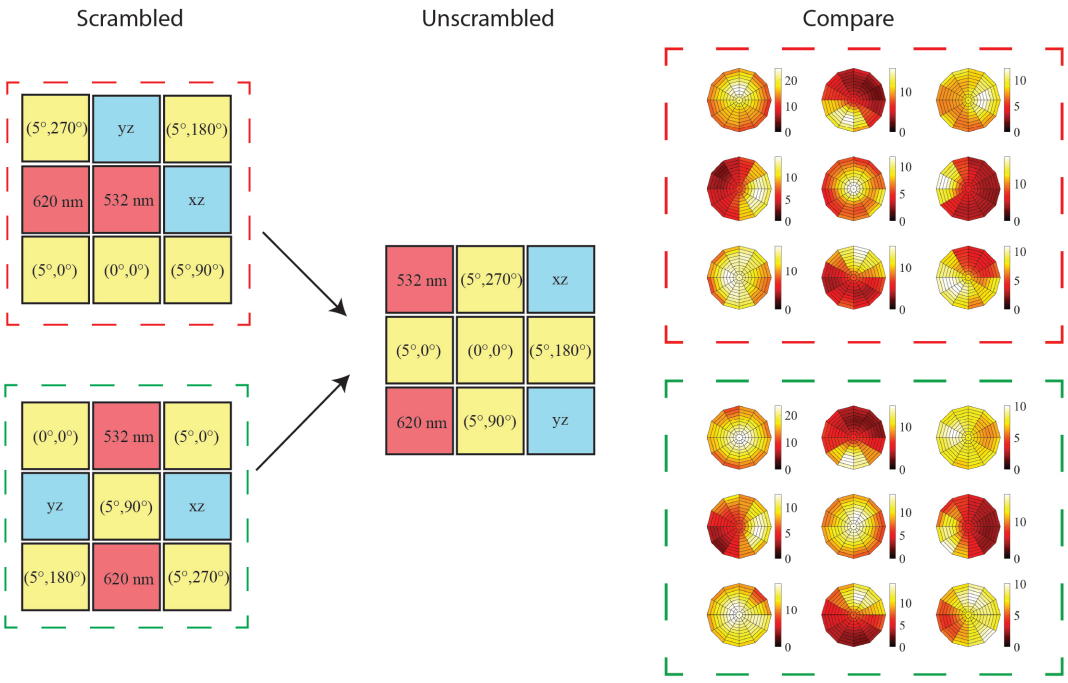

Figure S9: The procedure for studying qualitative similarity for two different pixel distributions, studying the worst case overlap from Fig. 4 of the main manuscript, which occurs in the yz-polarized pixel here. The distributions are unscrambled back to the original orientation for easy direct comparison of the angular responses for each pixel.

S8 Supplementary videos

The videos provided as individual files show the electric field intensity at the focal plane of the device presented in the main manuscript. Each video shows how the output electric field power changes as the polarization, wavelength, and incident angle of the input fields are altered.

Visualization 1: The polarization is swept continuously from x-polarization to y-polarization for 532 nm normally incident light.

Visualization 2: The wavelength is swept continuously from 532 nm to 620 nm for y-polarized, normally incident light.

Visualization 3: The incident angle θ is swept continuously from $-7°$ to $+7°$ for xz-polarized, 532 nm light with an azimuth angle of $\phi = 0°$.

Visualization 4: The incident angle θ is swept continuously from $-7°$ to $+7°$ for xz-

polarized, 532 nm light with an azimuth angle of $\phi = 90°$.

References

(1) Ballew, C.; Roberts, G.; Zheng, T.; Faraon, A. Constraining Continuous Topology Optimizations to Discrete Solutions for Photonic Applications. *ACS Photonics* **2023**, *10*, 836–844.

(2) Vercruysse, D.; Sapra, N. V.; Su, L.; Trivedi, R.; Vučković, J. Analytical level set fabrication constraints for inverse design. *Scientific Reports* **2019**, *9*, 1–7.